Title
Model-Interpolated Gating for Magnetic Resonance Image–Guided Radiation Therapy

Journal
International Journal of Radiation Oncology • Biology • Physics, 102(4)

ISSN
0360-3016

Authors
Ginn, John S
O'Connell, Dylan
Thomas, David H
et al.

Publication Date
2018-11-01

DOI
10.1016/j.ijrobp.2018.05.012

Peer reviewed

HHS Public Access

Author manuscript

Int J Radiat Oncol Biol Phys. Author manuscript; available in PMC 2019 November 15.

Published in final edited form as:

Int J Radiat Oncol Biol Phys. 2018 November 15; 102(4): 885–894. doi:10.1016/j.ijrobp.2018.05.012.

Model-Interpolated Gating for Magnetic Resonance Image—Guided Radiation Therapy

John S. Ginn, BS[*], **Dylan O'Connell, MS**[*], **David H. Thomas, PhD**[†], **Daniel A. Low, PhD**[*], and **James M. Lamb, PhD**[*]

[*]Department of Radiation Oncology, David Geffen School of Medicine, University of California, Los Angeles, Los Angeles, California

[†]Department of Radiation Oncology, University of Colorado School of Medicine, University of Colorado, Aurora, Colorado

Abstract

Purpose—To develop and validate a technique for radiation therapy gating using slow (≤1 frame per second) magnetic resonance imaging (MRI) and a motion model. Proposed uses of the technique include radiation therapy gating using T2-weighted images and conducting additional imaging studies during gated treatments.

Methods and Materials—The technique uses a physiologically guided breathing motion model to interpolate deformed target position between 2-dimensional (2D) MRI images acquired every 1 to 3 seconds. The model is parameterized by a 1-dimensional respiratory bellows surrogate and is continuously updated with the most recently acquired 2D images. A phantom and 8 volunteers were imaged with a 0.35T MRI-guided radiation therapy system. A balanced steady-state free precession sequence with a 2D frame rate of 3 frames per second was used to evaluate the technique. The accuracy and beam-on positive predictive value (PPV) of the model-based gating decisions were evaluated using the gating decisions derived from imaging as a ground truth. A T2-weighted gating offline proof-of-concept study using a half-Fourier, single-shot, turbo-spin echo sequence is reported.

Results—Model-interpolated gating accuracy, beam-on PPV, and median absolute distances between model and image-tracked target centroids were, on average, 98.3%, 98.4%, and 0.33 mm, respectively, in the balanced steady-state free precession phantom studies and 93.7%, 92.1%, and 0.86 mm, respectively, in the volunteer studies. T2 model-interpolated gating in 6 volunteers yielded an average accuracy and PPV of 94.3% and 92.5%, respectively, and the mean absolute median distance between modeled and imaged target centroids was 0.86 mm.

Conclusions—This work demonstrates the concept of model-interpolated gating for MRI-guided radiation therapy. The technique was found to be potentially sufficiently accurate for

Reprint requests to: John S. Ginn, BS, UCLA Radiation Oncology, 200 Medical Plaza, Suite B265, Los Angeles, CA 90095. Tel: (310) 267-3168; jginn@mednet.ucla.edu.

Conflict of interest: J.L., J.G. and D.L. are connected with the provisional patent application related to this work has been submitted. J.L. has previously received speaking and consulting fees from ViewRay. The authors report no other conflict of interest.

Supplementary material for this article can be found online at https://doi.org/10.1016/j.ijrobp.2018.05.012.

clinical use. Further development is needed to accommodate out-of-plane motion and the use of an internal MR-based respiratory surrogate

Introduction

Breathing motion degrades radiation therapy targeting accuracy and can result in tumor underdosing and critical structure overdosing. Established motion management techniques include use of a 4-dimensional computer tomography (4D-CT)—based internal target volume (1, 2) and gating based on external surrogates of tumor motion (3, 4) or internally implanted fiducial markers (5, 6). Magnetic resonance image (MRI)—guided radiation therapy is a relatively new technology that provides, among several potential benefits, an opportunity to improve motion management by gating the beam based on imaged target position (7–10). The ViewRay MRIdian (ViewRay, Inc Oakwood Village, OH) supports real-time respiratory gating by acquiring images using a balanced steady-state free precession sequence (bSSFP) in a single sagittal plane at approximately 4 frames per second or 3 sagittal planes at 2 frames per second. Targets are tracked using deformable image registration. The beam is held if the proportion of the target contour area outside a specified gating boundary contour exceeds a specified threshold. A more detailed description of the gating algorithm and clinical workflow at our institution can be found elsewhere (8).

A limitation of image-based respiratory gating is the requirement that the image frame rate must be rapid with respect to the breathing cycle to avoid unacceptably long gating latency (11). This constraint limits the selection of pulse sequences and thereby image contrasts that can be used for gating. For example, T2-weighted images require >1 second intervals between image acquisitions because of the relatively long duration of longitudinal relaxation (T1). However, T2-weighted images may provide superior image contrast for some tumors. T2-weighted images are useful for liver cancer detection (12), specifically assisting in both delineating and characterizing cholangiocarcinoma (13, 14). T2 images also provide better contrast for lung squamous cell carcinoma and adenocarcinoma (15).

We present a technique whereby a breathing motion model is used to interpolate the information necessary for a gating decision (“beam-on” vs “beam-off”) between images acquired at a low frame rate. The respiratory motion model establishes a physiologically guided correlation between respiratory motion and a respiratory surrogate. In this study, the model is built and continuously updated based on a sliding window of the most recently acquired low-frame-rate images. The model is used to determine the gating decision for any surrogate value until the next low-frame-rate image is acquired, thereby reducing the gating latency. The purpose of this article is to describe and validate this technique, which we refer to as model-interpolated gating (MI gating) and to report an offline proof-of-concept study using T2-weighted images for MRI-guided radiation therapy at 0.35 T.

Methods and Materials

Phantom and human volunteer images were acquired using the ViewRay MRIdian (ViewRay, Inc, Oakwood Village, OH) under an institutional review board—approved research protocol. The MRIdian combines a 0.35T split bore magnet with a ^{60}Co radiation

therapy system, enabling real-time MRI during radiation therapy. More details regarding the construction of the MRIdian can be found elsewhere (16, 17). The MRIdian uses a Siemens-sourced image acquisition and reconstruction system interfaced with the ^{60}Co radiation therapy system to perform imaging during treatment. A limited set of predefined imaging protocols is available in clinical mode. In research mode the 2 systems are disconnected and the Siemens control console is operated independently. Research mode enables the user to modify sequence parameters as desired and to upload additional pulse sequences for use during research mode. All imaging was performed in research mode.

Imaging protocols

We used bSSFP imaging to evaluate the accuracy of our technique and T2-weighted imaging to demonstrate a proof of concept of the technique. In this section we provide details of the imaging protocols.

bSSFP (18) single-plane 2Dsagittal images were acquired of a phantom and 8 volunteers at 3 frames per second (fps). Acquisition parameters included a 4.5 mm slice thickness, 2 × 2 mm^2 in-plane resolution, 400 × 400 mm^2 field of view (FOV), 1.38 milliseconds echo time (TE), 3.26 milliseconds repetition time (TR), 556 Hz/Px bandwidth, 60° flip angle, and 1 average. This protocol also implemented phase partial-Fourier and generalized autocalibrating partially parallel acquisition (GRAPPA) (19) techniques to reduce acquisition time (partial-Fourier factor of 6/8 and GRAPPA factor of 2). The same 2D gradient nonlinearity distortion corrections provided by Siemens that are used clinically were applied. As mentioned above, imaging was conducted in research mode. The most frequently used clinical imaging protocol uses a 5.0 mm slice thickness, 3.5 × 3.5 mm^2 in-plane resolution, 350 × 350 mm^2 FOV, 1.09 milliseconds TE, 2.49 milliseconds TR, 1000 Hz/Px bandwidth, 60° flip angle, 2 averages, partial-Fourier factor of 6/8, and GRAPPA factor of 2 along with the aforementioned distortion corrections to obtain images at approximately 4 fps.

AT2-weighted, half-Fourier, single-shot turbo spin echo (HASTE) sequence was used to obtain images of 6 of the volunteers that were scanned using the bSSFP sequence during normal breathing (the sequence was not available until after our first volunteer study, and the T2 study was not performed in 1 of the other volunteers). The Siemens source code for the sequence was modified by our group for use on the ViewRay MRIdian. Acquisition parameters included a 7 mm slice thickness, 3.5 × 3.5 mm^2 in plane resolution, 488 × 488 mm^2 FOV, 32 milliseconds TE, 3000 milliseconds TR, 751 Hz/Px bandwidth, and 1 average. The data acquisition duration for each individual image was 263 milliseconds to minimize motion blurring, with a 3 second delay between acquisitions (TR) to preserve T2-weighted contrast. Siemens-provided 2D distortion corrections were applied.

Respiratory bellows surrogate

A respiratory pneumatic bellows (Lafayette Instrument, Lafayette, IN) was attached to the phantom and the volunteers during the imaging studies. A transducer converted the bellows pressure to a voltage signal that was recorded during imaging using LabVIEW (Austin, TX) on an external computer. Synchronization of the bellows to the MRI scanner’s clock was

performed by correlating the bellows to an image-based respiratory surrogate as follows. A 2D fast-Fourier transform (FFT) of a manually selected portion of the image containing anatomic motion was performed. The center inferior—superior line of the resulting 2D FFT was then Fourier transformed back to the image domain to obtain a 1D image projection of each image. The first acquired 1D image projection was selected as a reference. The inferior—superior shift between each projection and the reference was determined by maximizing a correlation coefficient. This shift was used as the imaging surrogate. The respiratory bellows signal was aligned to this imaging surrogate by finding the temporal offset that maximized the correlation coefficient between the 2 surrogates. This process is summarized and an example is shown in Figure E1 (available online at https://doi.org/10.1016/j.ijrobp.2018.05.012). A Savitzky-Golay filter was used to reduce noise in the bellows surrogate, resulting in a 0.1 second temporal phase shift of the bellows surrogate relative to the image acquisition (20).

Phantom studies

An MRI-compatible motion phantom (CIRS, Inc, Norfolk, VA) was used to simulate inferior—superior respiratory motion. The phantom was composed of a large static cylindrical body, which held a sliding target section containing multiple trackable features that were made to move freely in the longitudinal direction. Two motion waveforms were used for the phantom studies: a $\cos^6$ wave with a 6-second period and 20-mm peak-to-peak amplitude, and a patient breathing waveform obtained by deformable tracking of a patient's tumor during MRI-guided treatment. The duration of the latter waveform was approximately 15 minutes, with a 95th to 5th percentile motion amplitude of 9.8 mm. An image of the phantom's motion rod and a portion of the realistic waveform used to drive the inferior—superior motion of the phantom can be seen in Figure 1. A series of 2000 bSSFP images was acquired continuously over a duration of approximately 11 minutes for each waveform.

Volunteer studies

Eight healthy volunteers were imaged to evaluate model-interpolated gating in vivo. Informed consent and Institutional Review Board approval were obtained. All imaging was conducted in the sagittal plane at a single slice position with well-visualized abdominal respiratory motion. A normal liver anatomic feature or the gallbladder was used to simulate tumor gating. A series of 2000 bSSFP images was acquired for all 8 volunteers, and a series of 200 T2-weighted images was acquired for 6 volunteers.

Image registration

For each image series, all images were deformably registered to a manually selected reference image using multi-level b-spline deformable registration with the Elastix package (21–23). Mutual information was used as the similarity metric. A bilateral filter was used on all images before registration to reduce the influence of noise. For the phantom studies, to avoid registration errors at the boundary of the motion rod caused by the static portion of the phantom, images were cropped before registration was performed. Registration accuracy was evaluated as follows. For each study, the same anatomic feature used as a simulated gating target was used as a landmark for registration accuracy evaluation. The position of the target in the reference image and first 100 registered images was manually identified. The

median distance of the registered target from the reference target (accuracy) and the median distance from the mean registered target position (consistency) were evaluated.

Motion modeling

Motion modeling was performed with custom software written in the MATLAB environment (MathWorks, Natick, MA). The deformation vector fields obtained from image registration were used to fit the model parameters of the previously validated 5-dimensional linear motion model (24–27):

$$\vec{x} = \vec{\alpha} v + \vec{\beta} f + \vec{x_0} \quad (1)$$

where $\vec{x}$ is the estimated tissue position, $\vec{\alpha}$ and $\vec{\beta}$ are voxel-specific model parameters representing the correlation between tissue position and the surrogate amplitude v and airflow rate f, and $\vec{x_0}$ is the voxel-specific initial tissue position. The bellows voltage and voltage time derivative served as the amplitude and airflow rate surrogates, respectively. The parameters $\vec{\alpha}$, $\vec{\beta}$, and $\vec{x_0}$ were fit using least-squares minimization.

Model-interpolated gating algorithm

The model-interpolated gating algorithm using low-frame-rate images is described as follows:

1. A reference image for registration is manually selected. This image is also used to create the initial target contour.
2. The target contour is generated at an end exhale breathing phase and is expanded automatically by the specified margin to form the gating boundary.
3. The most recently acquired N images are deformably registered to the reference image. The resulting deformation vector fields and corresponding bellows surrogate values are used to build the model.
4. The surrogate value is used continuously with the model to estimate tissue motion and deform the target contour prospectively until the next image is acquired.
5. If the model-deformed target contour extends outside the gating boundary by a prespecified percent excursion, the gating decision is “beam off.” Otherwise, the gating decision is “beam on.”
6. The model is updated using a sliding window of the N most recently acquired images.
7. Steps 3 to 6 are repeated for the duration of beam gating.

MI gating evaluation using bSSFP images

The MI gating was evaluated using bSSFP images acquired at 3 fps. The use of low-frame-rate images was simulated by using only every i^{th} image to build the model (i = 4 or 10). The next skipped images (i.e., the next 3 or 9 images not used for model building) were used to compare the MI gating decision with the direct-image-based gating decision, which was assumed to be the criterion standard. Figure 2 shows a schematic representation of the accuracy evaluation method using every fourth image to build the model (i = 4). Accuracy and positive predictive value (PPV) were quantified. Accuracy was defined as the fractional percentage agreement between MI gating decisions and direct-image gating decisions. PPV was defined as the proportion of the model gating decisions that were correct when the model decision was “beam on.” Additionally, the absolute distance between modeled and imaged target centroids was quantified. The median, standard deviation, and 95th percentile model and image centroid absolute distances were calculated for all gating comparisons, and separately for only model false positives (when the MI gating decision was “beam-on” but the direct image gating decision was “beam-off”). A range of variations in gating boundary margin expansion, number, and temporal spacing of images used to build the model were explored to test MI gating sensitivity to these parameters. A paired Student t test was performed to evaluate whether or not the change in any given parameter yielded a statistically significant difference in gating accuracy or PPV.

Proof-of-concept using T2-weighted images

An offline proof-of-concept T2-weighed gating study was conducted by fitting the motion model using 10 consecutively acquired images, comparing MI gating and direct image gating at the next acquired image. The model was subsequently updated following the gating evaluation. The MI gating accuracy and PPV are reported using a 3 mm gating margin and 10% excursion tolerance (ie, the percentage of the target allowed outside the gating boundary before the beam is turned off). The median, standard deviation, and 95th percentile absolute distances between model and image centroids are reported for all gating comparisons and separately for model false positives.

Results

Gating accuracy evaluation using bSSFP images

Model-interpolated gating accuracy, beam-on PPV, and median absolute distance between the model and image centroids were, on average, 98.3%, 98.4%, and 0.33 mm, respectively, in the bSSFP phantom studies and 93.7%, 92.1%, and 0.86 mm, respectively, in the bSSFP volunteer studies. An example comparison of model-interpolated and direct-image gating is shown in Figure 3, and a video corresponding to this example can be found with the supplementary materials online (available at https://doi.org/10.1016/j.ijrobp.2018.05.012). Table 1 shows all bSSFP comparisons between model-based and image-based gating using a model built from 10 images spaced 3.19 seconds apart (ie, using every 10th acquired image to build the model, and the 9 subsequent images to evaluate MI gating accuracy) for a 3 mm gating margin and 10% gating excursion tolerance. Gating parameters had little impact on the MI gating accuracy in the volunteer studies. The following comparisons used the parameters reported above unless otherwise specified. Increasing the temporal spacing

between images used to build the model from 1.27 to 3.19 seconds reduced gating accuracy and PPV, on average, by 1.74% and 2.50%, respectively. Increasing the number of training images from 10 to 30 while holding the temporal spacing between images constant reduced gating accuracy and PPV, on average, by 0.50% and 1.00%, respectively. Expanding the margins from 3 mm to 5 mm improved gating accuracy and PPV, on average, by 0.49% and 2.76%, respectively. A paired Student t test revealed that none of the changes in gating parameters resulted in a statistically significant difference in gating accuracy or PPV.

Gating accuracy evaluation with T2-contrast images

For the T2 image series, using a 3 mm target margin, 10% target excursion tolerance and 10 images to train the motion model yielded an average gating accuracy, PPV, and median absolute distance between model and image centroids of 94.3%, 92.5%, and 0.86 mm, respectively, across the 6 volunteers. Table 2 shows the T2-model gating results for each of the volunteers using a model built from 10 images, a gating margin of 3 mm, and a gating tolerance of 10%. Figure 4 shows the bSSFP and T2-weighted half-Fourier single-shot turbo spin echo images obtained from 1 of the volunteers. No formal process was performed to select sequence parameters so as to optimize T2 contrast. However, the gallbladder and kidney are more visible in the T2-weighted image.

Registration accuracy

Registration median accuracy and consistency were, on average, subvoxel for all volunteer studies. The median registration accuracy and consistency were, on average, 1.01 mm and 0.54 mm, respectively, in the bSSFP volunteer studies and 1.64 mm and 0.84 mm, respectively, in the T2 volunteer studies. Registration error may have been larger in the T2 registrations because of the larger voxel size.

Discussion

This work demonstrated that MI gating, or radiation therapy gating using a motion model to interpolate between low-frame-rate images, agreed well with gating directly on high-frame-rate images. Several evaluation metrics are reported in the results section. Accuracy was defined as the fractional percentage of agreement between MI gating decisions and direct-image gating decisions; an accuracy less than 100% indicates the possibility of either a reduction in duty cycle (false negative) or irradiation of tissue outside the intended target (false positive). The PPV metric indicates the fraction of time when the target is in the correct location when the beam is on (using direct image gating as a ground truth), corresponding to dosimetric feasibility. It should be noted that dose spillage outside the target is inevitable in photon radiation therapy even without respiratory motion and that further dose distribution blurring occurs even in direct image gating as a result of gating latency (8, 28). Modeled versus imaged target centroid differences are reported because they are an objective measure of model performance independent of application (i.e., specific gating parameters, such as margin and excursion tolerance). Finally, modeled versus imaged centroid differences for false positive gating decisions (i.e., the model incorrectly determines the beam should be on) are reported because they give an indication of the spatial magnitude

of error when the gating decision was incorrect. These values should be compared with spatial tolerances typically used clinically.

MI gating was robust to changes in gating parameters; none of the changes in parameters led to a statistically significant difference in gating accuracy or PPV. The largest average change resulted from increasing the gating margin from 3 mm to 5 mm, increasing accuracy and PPV by 0.49% and 2.76%. This was likely a result of the larger proportion of true positives (i.e., higher gating duty cycle resulting from larger gating margin). Model gating accuracy and PPV decreased, on average, by 0.50% and 1.00% when the number of training images used to build the model increased from 10 to 30. Incorporating more images enables more respiratory states to be included during modeling, but it decreases the rate at which the model can adapt to changes in breathing patterns. Gating accuracy and PPV averaged 94.0% and 92.2%, respectively, with an average absolute median distance between model and image target centroids of 0.86 mm across all studies.

In image-based gating as currently implemented in commercial MRI-guided radiation therapy systems, accurate gating requires images to be acquired rapidly with respect to the breathing cycle. Model-interpolated gating decreases the required frame rate to as low as 0.33 fps with a slight reduction in accuracy (average accuracy and PPV of 93.7% and 92.1% in the volunteer studies). The use of a lower frame rate allows T2-weighted image gating, which requires a long enough time between image acquisitions to allow for nearly complete T1 relaxation. Furthermore, model-interpolated gating could be used to allow the acquisition of additional imaging studies simultaneously with gated treatment (i.e., interleave functional imaging between low-frame-rate bSSFP imaging used for model-interpolated gating), potentially making it easier to incorporate daily functional imaging into routine treatment workflows (29–31). Alternatively, inasmuch as the respiratory surrogate is acquired continuously, MI gating could be used to decrease gating latency relative to even fast MRI imaging, potentially improving the dosimetric accuracy of gated treatments (11, 32). Incorporating MI gating in the clinical workflow is logistically feasible because it would extend treatment times only by the duration required to obtain the first set of training images (e.g., 10 training images spaced 3 seconds apart would require 30 seconds). The respiratory bellows would need to be considered in treatment planning during a clinical implementation of MI gating. The bellows are visible in the MRI images and could be incorporated in the planning workflow in a manner similar to the way treatment couches and immobilization devices are included in dose calculations.

A short computation time is necessary to avoid introducing additional gating latency. Our work was performed with a central processing unit, largely single-thread implementation in MATLAB. For 1 volunteer, fitting the models required to describe the target contour took, on average, a total of 0.003 seconds. Once the surrogate was obtained, deforming the contour and computing the gating decision using the model took, on average, a total of 0.004 seconds. A clinical implementation of the proposed method could be performed on a graphics processing unit to further reduce computation time by exploiting the fact that all points are modeled independently.

The technique of MI gating is subject to some limitations. Model accuracy may be reduced if the surrogate or tissue motion lies outside the training range used to build the model, or in the case of large out-of-plane motion. Out-of-plane motion could be addressed by implementing a slice-to-volume registration algorithm, but that remains a work in progress. These issues are not limited to model-based interpolation: direct image-based gating may also lose accuracy in cases of unusually large breaths, large out-of-plane motion, or both. Model inaccuracy may also result from a change in the correlation between the respiratory surrogate and anatomic motion during treatment. Updating the motion model using a sliding window allows the model to accommodate slow changes in breathing pattern and correspondence between internal and external motion. However, it is more difficult for the model to quickly adjust to rapid changes in the correspondence between the surrogate and anatomic motion (e.g., if the bellows shifts positions or if the patient moves). For example, during both the bSSFP and T2 Volunteer 6 studies, the volunteer stretched and changed the way they breathed during the study (e.g., predominantly abdominal breathing vs chest breathing). These changes were associated with a reduced correlation coefficient between the bellows and the image-derived surrogate used for bellows alignment and with a reduced gating accuracy and PPV compared with those reported in the other studies. The use of a correlation coefficient—based beam veto to increase PPV is under study but is beyond the scope of the present study. Recent work indicates that the correlation between the respiratory surrogate and anatomic motion could be improved by providing audiovisual feedback, and it may help to avoid sudden voluntary motion (33). Our current work uses a bellows as a respiratory surrogate, but our technique is generalizable to the use of other surrogates such as a navigator echo. Using a respiratory bellows enables a rapid, continuous acquisition of the respiratory surrogate without the need for additional pulse sequence modifications that may slow down or interfere with image acquisition (34).

Previous works using motion models in MRI-guided radiation therapy have primarily focused on predicting tumor position (35–37) and on estimating tumor motion in 3 dimensions by building a motion model using multiple orthogonal imaging planes (38, 39). Correlative motion models such as ours have also been proposed in the context of multileaf collimator tracking (40). Our proposed technique bears similarities to the correlation method used by the Cyberknife Synchrony respiratory tracking system (41).

Significant differences from the Cyberknife system include the following. First, our technique is able to predict the locations of arbitrary points in the imaged plane, whereas Synchrony predicts the locations of discrete points; in fact, our technique could be easily extended to 3D with 3D images acquired using novel rapid 3D imaging techniques (42). Second, our technique can be used to produce synthetic images at arbitrary breathing phases, as shown in Figure 3. Third, because our technique uses MRI instead of planar kV x-ray imaging, the model is updated every 1 to 4 seconds, compared with typically 1 to 5 minutes between updates with the Synchrony system (43), which potentially leads to greater robustness to changes in breathing patterns. The Cyberknife Xsight lung does allow continuous 2D tracking of tumors that are visible in the treatment beam image; however, this is possible only for 20% to 40% of lung tumors (44). Fourth, our technique incorporates prior knowledge of possible tissue trajectories through a biomechanically motivated breathing motion model that acts to constrain the correlation between tissue motion and

breathing surrogate, and it may be more accurate than correlation models alone. It has been reported that 6.9 mm and 4.6 mm treatment margins in the inferior—superior and anteroposterior directions, respectively, is required to account for 95% of tracking error when the Synchrony system is used (45). In our work, the 95th percentile model and image centroid absolute difference in the sagittal plane was, on average, 2.85 mm in the bSSFP studies and 2.96 mm in the T2 studies. In our implementation, we have used the 5-dimensional motion model, but many other lung motion models exist (46–49), and some of them could be used equivalently for MI-gating.

Conclusions

This work demonstrates that radiation therapy gating using a motion model agrees well with gating directly on high-frame-rate images. Model-interpolated gating could potentially enable the use of frame-rate-limited pulse sequences for radiation therapy gating and allow the acquisition of additional imaging studies during gated radiation therapy. Further development is needed to accommodate out-of-plane motion and the use of an internal MR-based respiratory surrogate.

Supplementary Material

Refer to Web version on PubMed Central for supplementary material.

Acknowledgments

Supported in part by a National Institutes of Health grant (2T32EB2101–41).

References

1. Slotman BJ, Lagerwaard FJ, Senan S, et al. 4D imaging for target definition in stereotactic radiotherapy for lung cancer. Acta Oncol 2006;45:966–972. [PubMed: 16982565]
2. Loo BW Jr., Kavanagh BD, Meyer JL, et al. Motion management and image guidance for thoracic tumor radiotherapy: Clinical treatment programs. Fron Radiat Ther Oncol 2011;43:271–291.
3. Wagman R, Yorke E, Ford E, et al. Respiratory gating for liver tumors: Use in dose escalation. Int J Radiat Oncol Biol Phys 2003;55:659–668. [PubMed: 12573753]
4. Giraud P, Yorke E, Ford EC, et al. Reduction of organ motion in lung tumors with respiratory gating. Lung Cancer 2006;51:41–51. [PubMed: 16198022]
5. Shirato H, Shimizu S, Kunieda T, et al. Physical aspects of a real-time tumor-tracking system for gated radiotherapy. Int J Radiat Oncol Biol Phys 2000;48:1187–1195. [PubMed: 11072178]
6. van der Voort van Zyp NC, Prevost JB, Hoogeman MS, et al. Stereotactic radiotherapy with real-time tumor tracking for non-small cell lung cancer: Clinical outcome. Radioth Oncol 2009;91:296–300.
7. Crijns SP, Kok JG, Lagendijk JJ, et al. Towards MRI-guided linear accelerator control: Gating on an MRI accelerator. Phys Med Biol 2011;56:4815–4825. [PubMed: 21753236]
8. Lamb JM, Ginn JS, O'Connell DP, et al. Dosimetric validation of a magnetic resonance image gated radiotherapy system using a motion phantom and radiochromic film. Journal of applied clinical medical physics 2017;18:163–169.
9. Crijns SP, Raaymakers BW, Lagendijk JJ, et al. Proof of concept of MRI-guided tracked radiation delivery: Tracking one-dimensional motion. Phys Med Bio 2012;57:7863–7872. [PubMed: 23151821]

10. Yun J, Wachowicz K, Mackenzie M, et al. First demonstration of intrafractional tumor-tracked irradiation using 2D phantom MR images on a prototype linac-MR. Med Phys 2013;40:051718. [PubMed: 23635266]
11. Keall PJ, Mageras GS, Balter JM, et al. The management of respiratory motion in radiation oncology report of AAPM task group 76. Med Phys 2006;33:3874–3900. [PubMed: 17089851]
12. Liu Y, Yin FF, Czito BG, et al. T2-weighted four dimensional magnetic resonance imaging with result-driven phase sorting. Med Phys 2015;42:4460–4471. [PubMed: 26233176]
13. Chung YE, Kim MJ, Park YN, et al. Varying appearances of cholangiocarcinoma: Radiologic-pathologic correlation. Radiographics 2009;29:683–700. [PubMed: 19448110]
14. Maetani Y, Itoh K, Watanabe C, et al. MR imaging of intrahepatic cholangiocarcinoma with pathologic correlation. AJR Am J Roentgenol 2001;176:1499–1507. [PubMed: 11373220]
15. Freedman JN, Collins DJ, Bainbridge H, et al. T2-weighted 4Dmagnetic resonance imaging for application in magnetic resonance guided radiotherapy treatment planning. Invest Radiol 2017;52:563–573. [PubMed: 28459800]
16. Ginn JS, Agazaryan N, Cao M, et al. Characterization of spatial distortion in a 0.35 t mri-guided radiotherapy system. Phys Med Biol 2017;62:4525–4540. [PubMed: 28425431]
17. Mutic S, Dempsey JF. The viewray system: Magnetic resonance guided and controlled radiotherapy. Semin Radiat Oncol 2014;24:196–199. [PubMed: 24931092]
18. Scheffler K, Lehnhardt S. Principles and applications of balanced SSFP techniques. Eur Radiol 2003;13:2409–2418. [PubMed: 12928954]
19. Griswold MA, Jakob PM, Heidemann RM, et al. Generalized auto-calibrating partially parallel acquisitions (GRAPPA). Magn Reson Med 2002;47:1202–1210. [PubMed: 12111967]
20. Savitzky A, Golay MJE. Smoothing and differentiation of data by simplified least squares procedures. Anal Chem 1964;36:1627–1639.
21. Klein S, Pluim JPW, Staring M, et al. Adaptive stochastic gradient descent optimisation for image registration. Int J Comp Vis 2009;81:227.
22. Shamonin DP, Bron EE, Lelieveldt BP, et al. Fast parallel image registration on CPU and GPU for diagnostic classification of Alzheimer's disease. Front Neuroinform 2014;7:50. [PubMed: 24474917]
23. Klein S, Staring M, Murphy K, et al. Elastix: A toolbox for intensity-based medical image registration. IEEE Trans Med Imaging 2010;29: 196–205. [PubMed: 19923044]
24. Low DA, Parikh PJ, Lu W, et al. Novel breathing motion model for radiotherapy. Int J Radiat Oncol Biol Phys 2005;63:921–929. [PubMed: 16140468]
25. O'Connell DP,Thomas DH,Dou TH, et al.Comparison of breathing gated ct images generated using a 5dct technique and a commercial clinical protocol in a porcine model. Medical Physics 2015;42:4033–4042. [PubMed: 26133604]
26. Dou TH, Thomas DH, O'Connell DP, et al. A method for assessing ground-truth accuracy of the 5dct technique. Int J Radiat Oncol Biol Phys 2015;93:925–933. [PubMed: 26530763]
27. Thomas D, Lamb J, White B, et al. A novel fast helical 4d-ct acquisition technique to generate low-noise sorting artifact–free images at user-selected breathing phases. Int J Radiat Oncol Biol Phys 2014;89: 191–198. [PubMed: 24613815]
28. Smith WL, Becker N. Time delays in gated radiotherapy. J Appl Clin Med Phys 2009;10:2896. [PubMed: 19692973]
29. Mahmood F, Johannesen HH, Geertsen P, et al. Repeated diffusion MRI reveals earliest time point for stratification of radiotherapy response in brain metastases. Phys Med Biol 2017;62:2990–3002. [PubMed: 28306548]
30. Shaverdian N, Yang Y, Hu P, et al. Feasibility evaluation of diffusion-weighted imaging using an integrated MRI-radiotherapy system for response assessment to neoadjuvant therapy in rectal cancer. Br J Radiol 2017;90:20160739. [PubMed: 28079398]
31. Yang Y, Cao M, Sheng K, et al. Longitudinal diffusion MRI for treatment response assessment: Preliminary experience using an MRI-guided tricobalt 60 radiotherapy system. Med Phys 2016;43:1369–1373. [PubMed: 26936721]

32. Bjerre T, Crijns S, af Rosenschold PM, et al. Three-dimensional MRI-linac intra-fraction guidance using multiple orthogonal cine-MRI planes. Phys Med Biol 2013;58:4943–4950. [PubMed: 23807514]
33. Lee D, Greer PB, Paganelli C, et al. Audiovisual biofeedback improves the correlation between internal/external surrogate motion and lung tumor motion. Med Phys 2018;45:1009–1017. [PubMed: 29360149]
34. Santelli C, Nezafat R, Goddu B, et al. Respiratory bellows revisited for motion compensation: Preliminary experience for cardiovascular MR. Magn Reson Med 2011;65:1097–1102. [PubMed: 21413074]
35. Bourque AE, Carrier J-F, Filion É, et al. A particle filter motion prediction algorithm based on an autoregressive model for real-time MRI-guided radiotherapy of lung cancer. Biomed Phys Eng Expr 2017;3:035001.
36. Sharp GC, Jiang SB, Shimizu S, et al. Prediction of respiratory tumour motion for real-time image-guided radiotherapy. Phys Med Biol 2004; 49:425–440. [PubMed: 15012011]
37. Cervino LI, Du J, Jiang SB, et al. MRI-guided tumor tracking in lung cancer radiotherapy. Phys Med Biol 2011;56:3773–3785. [PubMed: 21628775]
38. Stemkens B, Tijssen RH, de Senneville BD, et al. Image-driven, model-based 3D abdominal motion estimation for MR-guided radiotherapy. Phys Med Biol 2016;61:5335–5355. [PubMed: 27362636]
39. Seregni M, Paganelli C, Lee D, et al. Motion prediction in MRI-guided radiotherapy based on interleaved orthogonal cine-MRI. Phys Med Biol 2016;61:872–887. [PubMed: 26740517]
40. Sawant A, Venkat R, Srivastava V, et al. Management of three-dimensional intrafraction motion through real-time DMLC tracking. Med Phys 2008;35:2050–2061. [PubMed: 18561681]
41. Kilby W, Dooley JR, Kuduvalli G, et al. The cyberknife robotic radiosurgery system in 2010. Technol Cancer Res Treat 2010;9:433–452. [PubMed: 20815415]
42. Li G, Wei J, Kadbi M, et al. Novel super-resolution approach to time-resolved volumetric 4-dimensional magnetic resonance imaging with high spatiotemporal resolution for multi-breathing cycle motion assessment. Int J Radiat Oncol Biol Phys 2017;98:454–462. [PubMed: 28463165]
43. Kresl JJ, Urschel HC, Luketich JD, et al. Robotic Radiosurgery Treating Tumors That Move With Respiration. Berlin, Heidelberg: Springer-Verlag; 2007.
44. Fu D, Kahn R, Wang B, et al. Xsight lung tracking system: A fiducial-less method for respiratory motion tracking In: Urschel HC, Kresl JJ, Luketich JD, Papiez L, Timmerman RD, Schulz RA, editors. Treating Tumors that Move with Respiration, 1. Berlin, Heidelberg: Springer; 2007 p. 265.
45. Pepin EW, Wu H, Zhang Y, et al. Correlation and prediction uncertainties in the cyberknife synchrony respiratory tracking system. Med Phys 2011;38:4036–4044. [PubMed: 21859002]
46. McClelland JR, Hawkes DJ, Schaeffter T, et al. Respiratory motion models: A review. Med Image Anal 2013;17:19–42. [PubMed: 23123330]
47. McClelland JR, Chandler AG, Blackall JM, et al. 4d motion models over the respiratory cycle for use in lung cancer radiotherapy planning. Medical Imaging. SPIE. 2005 pp. 11.
48. Torshabi AE, Pella A, Riboldi M, et al. Targeting accuracy in real-time tumor tracking via external surrogates: A comparative study. Technol Cancer Res Treat 2010;9:551–562. [PubMed: 21070077]
49. King AP, Buerger C, Tsoumpas C, et al. Thoracic respiratory motion estimation from MRI using a statistical model and a 2D image navigator. Med Image Anal 2012;16:252–264. [PubMed: 21959365]

Summary

A model-interpolated gating algorithm was developed for magnetic resonance image—guided radiation therapy. A breathing motion model was used to deformably interpolate target position between magnetic resonance images acquired at low frame rates (≤1 frame per second). This technique enables radiation therapy gating based on pulse sequences that require long acquisition delays, such as T2-weighted sequences, potentially enhancing the accuracy of tumor targeting. Phantom and volunteer studies were conducted to evaluate the accuracy of model-interpolated gating compared with that of direct image gating.

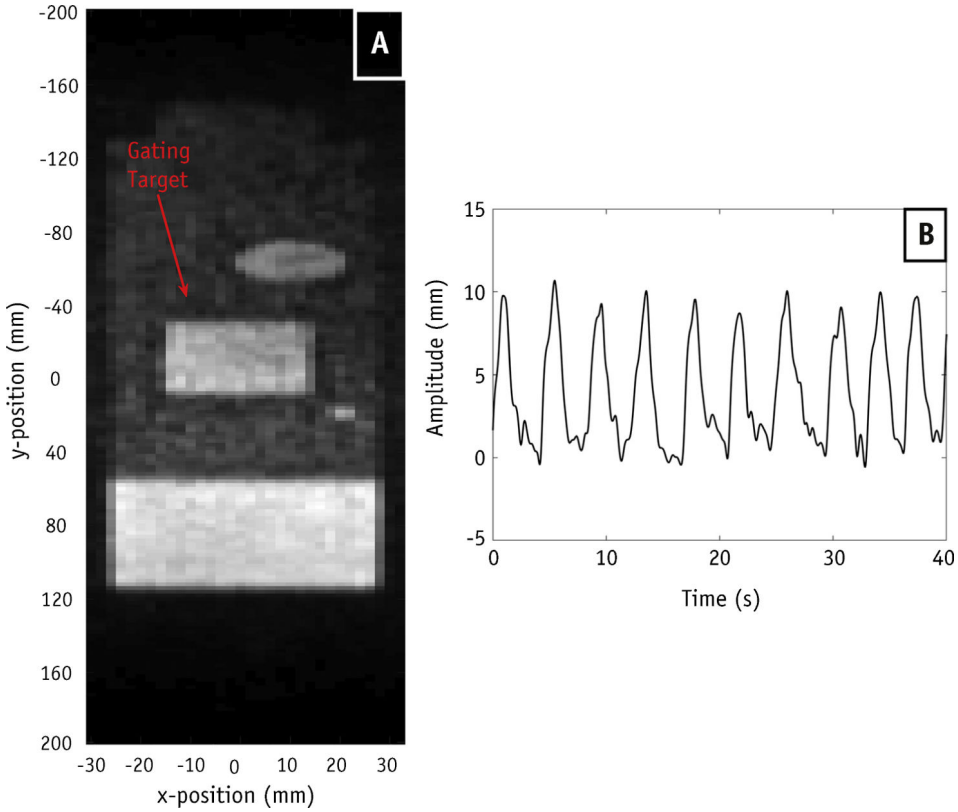

Fig. 1.

(A) Phantom's motion rod. (B) Realistic breathing waveform used to simulate inferior-superior anatomic motion.

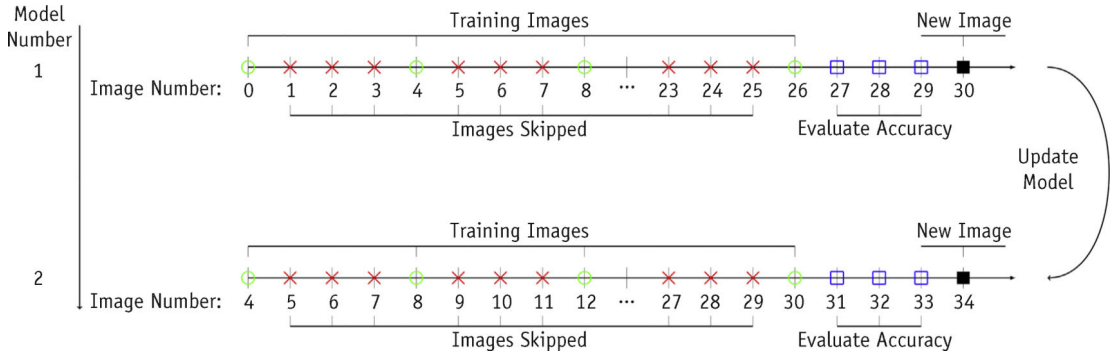

Fig. 2.

Example of the model interpolated (MI) gating accuracy evaluation using a sliding window of 10 images composed of every fourth image to build the model (open circles). Skipped images (crosses) are omitted from model building to simulate MI gating using training images obtained with a large temporal spacing (T2-weighted images). The accuracy of model gating is evaluated using the images marked with open squares. The model is then updated with a newly acquired image (solid square).

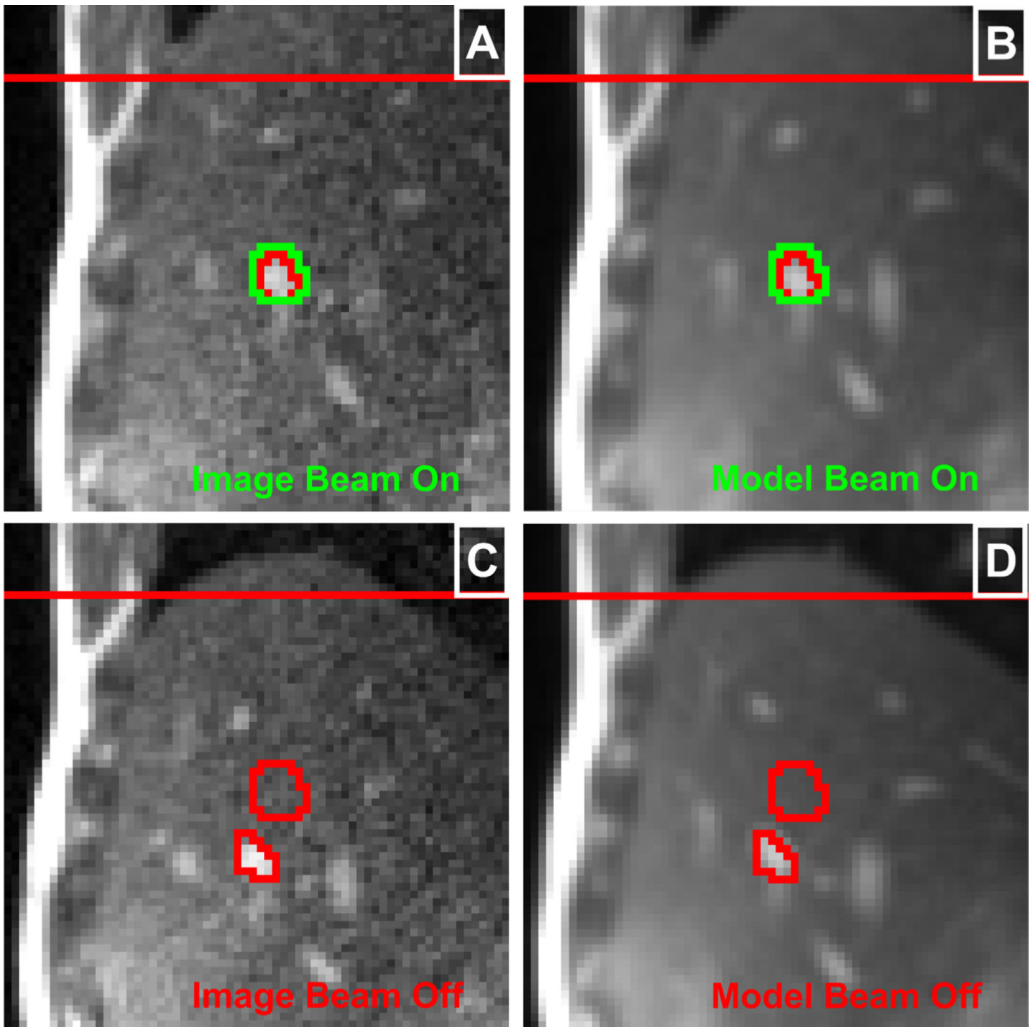

Fig. 3.

Example of balanced steady-state free precession image and model-based radiation therapy gating using a 3 mm contour margin and 10% excursion tolerance. A sliding window of 10 images, each separated by 3.19 seconds, was used to build the model. The surrogate values corresponding to the time the raw images (A, C) were acquired were used to generate the model images (B, D). The static contours show the gating boundary (which is fixed in space), and the moving smaller contours represent the tracked targets. The horizontal line serves as a reference to assist in visualizing respiratory motion.

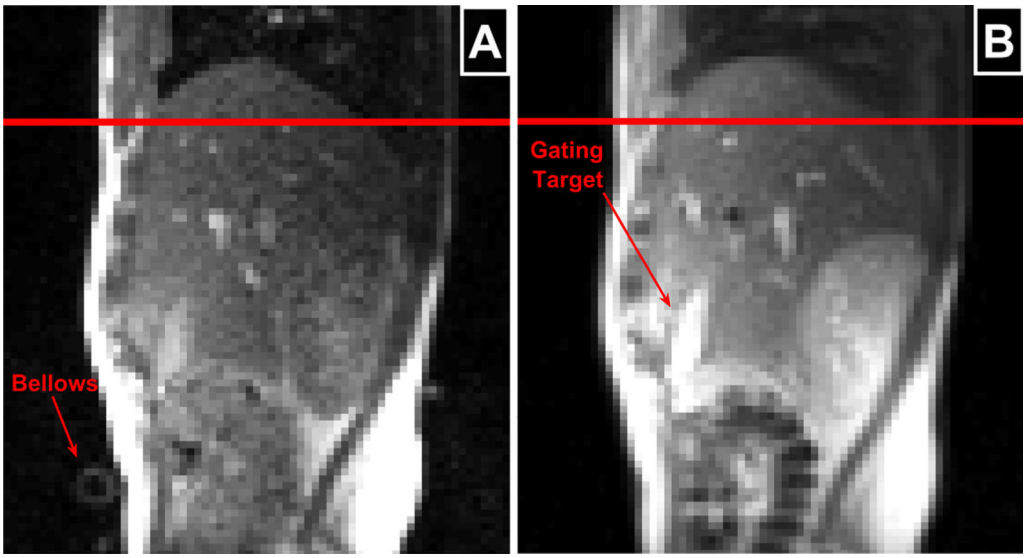

Fig. 4.

(A) Balanced steady-state free precession image interpolated to the same in-plane resolution as the T2-weighted half-Fourier single-shot turbo spin echo image (B) showing the gallbladder target region. The horizontal line serves as a reference to assist in indicating respiratory phase.

Table 1

Balanced steady-state free precession gating analysis comparing model and image-based gating using only images that were skipped during model fitting

Study	Accuracy (%)	Positive predictive value (%)	Direct image gating duty cycle (%)	95th to 5th percentile image centroid motion (mm)	Model and image centroid distance (mm)					
					All images			False positive gating decisions		
					Median	Standard deviation	95th percentile	Median	Standard deviation	95th percentile
Phantom										
Artificial	99.2	98.9	63.6	19.7	0.40	0.23	0.83	0.68	0.35	1.28
Realistic	97.3	97.8	85.6	9.61	0.26	0.18	0.66	0.33	0.18	0.71
Volunteer 1	96.0	95.2	47.6	17.2	0.90	0.87	2.71	1.43	2.03	7.04
Volunteer 2	97.8	97.4	56.8	14.7	0.67	0.55	1.91	1.16	0.64	2.44
Volunteer 3	95.0	95.2	61.4	17.7	0.83	1.23	2.51	1.79	1.20	4.42
Volunteer 4	94.1	95.5	85.5	9.59	0.75	0.62	2.03	1.74	0.91	3.33
Volunteer 5	96.0	93.7	58.3	14.0	0.76	0.94	2.59	1.96	2.21	7.08
Volunteer 6	79.9	70.1	35.1	15.5	1.32	2.24	5.83	2.23	1.82	6.02
Volunteer 7	95.5	95.7	55.8	11.0	0.61	0.60	1.78	1.10	0.80	2.92
Volunteer 8	95.5	93.8	26.9	31.8	1.06	1.33	3.39	1.63	5.48	17.6

The model was built using every 10th image and a total of 10 images. The analysis was conducted with a 3 mm gating margin and 10% gating excursion tolerance. The accuracy and beam-on positive predictive value of model gating are reported. The 95th to 5th percentile image centroid motion and image gating duty cycle are given. The median, standard deviation, and 95th percentile of the modeled and imaged target centroid absolute distance for all evaluation images (ie, those excluded from model building) and only evaluation images corresponding to model false positives are reported.

Table 2

T2 gating analysis comparing model and image-based gating

Study	Accuracy (%)	Positive predictive value (%)	Direct image gating duty cycle (%)	95th to 5th percentile image centroid motion (mm)	Model and image centroid distance (mm)					
					All images			False positive gating decisions		
					Median	Standard deviation	95th percentile	Median	Standard deviation	95th percentile
Volunteer 2	96.3	97.7	92.1	7.28	0.58	0.49	1.77	1.43	0.88	2.08
Volunteer 4	92.1	96.4	89.5	6.06	0.75	0.90	2.35	1.62	0.84	3.12
Volunteer 5	93.7	90.7	52.6	14.2	0.73	1.57	3.98	2.37	1.45	4.58
Volunteer 6	92.1	77.8	21.1	13.3	1.21	2.10	4.63	2.12	1.22	4.63
Volunteer 7	94.2	95.6	71.6	7.67	0.65	0.43	1.65	1.09	0.75	2.24
Volunteer 8	97.4	96.6	31.1	25.7	1.24	0.93	3.35	2.00	0.19	2.14

The model was built with 10 consecutively acquired images. The analysis was conducted with a 3 mm gating margin and 10% gating excursion tolerance. The accuracy and beam-on positive predictive value of model gating are reported. The 95th to 5th percentile image centroid motion and image gating duty cycle are given. The median, standard, deviation and 95th percentile of the modeled and imaged target centroid absolute distance for all images and only images corresponding to model false positives are reported.

Int J Radiat Oncol Biol Phys. Author manuscript; available in PMC 2019 November 15.